Ultra-sensitive high aspect-ratio flexible optical fibers for multi-parameter high-resolution sensing

Pawel Maniewski

pawelma@kth.se

KTH Royal Institute of Technology https://orcid.org/0000-0003-0137-260X

Robin Hartley

University of Bristol

Timothy Lee

University of Southampton

Matthew Whitaker

University of Southampton

Bruno Moog

University of Southampton

Martynas Beresna

University of Southampton https://orcid.org/0000-0003-2427-3129

Janice Dulieu-Barton

University of Bristol

Christopher Holmes

University of Southampton

Article

Keywords:

Posted Date: May 2nd, 2025

DOI: https://doi.org/10.21203/rs.3.rs-6352437/v1

Additional Declarations: There is **NO** Competing Interest.

Ultra-sensitive high aspect-ratio flexible optical fibers for multi-parameter high-resolution sensing

Pawel Maniewski[1,2*] Robin Hartley[3], Timothy Lee[1], Matthew Whitaker[1], Bruno Moog[1], Martynas Beresna[1], Janice M. Dulieu-Barton[3], Christopher Holmes[1]

[1]Optoelectronic Research Centre, University of Southampton, Southampton, United Kingdom
[2]Department of Applied Physics, KTH Royal Institute of Technology, Stockholm, Sweden
[3]Bristol Composites Institute, University of Bristol, Bristol, United Kingdom

*Corresponding author: pawelma@kth.se

Abstract: A new class of optical fibers characterized by a high aspect ratio quadrilateral cross-section is introduced, termed high-aspect-ratio-flat-fiber (HARFF). HARFFs demonstrate superior performance in applications demanding an asymmetric, deterministic response, providing enhanced sensitivity, precision, and resilience. Using advanced laser-based processing combined with stack-and-draw fabrication, we engineered HARFFs with tailored mechanical properties, yielding ultra-sensitive pressure sensors with over three orders of magnitude improvement in sensitivity over conventional optical fiber designs. We demonstrated further sensitivity enhancement in HARFFs through a multi-material microstructure by achieving increased temperature sensitivity in Sn-alloy-filled HARFFs. Our findings highlight the transformative potential of HARFFs, opening new avenues for innovations in non-circular high aspect-ratio fiber optics.

1. Introduction

Advances in optical fiber technology have consistently driven transformative breakthroughs, reshaping industries and everyday life. By introducing advanced materials and novel designs, modern optical fibers continue to push boundaries, setting new standards and overcoming longstanding limitations[1–5]. Fiber sensors, in particular, have emerged as key enablers, offering enhanced precision, resilience, and versatility across a wide range of applications, from aerospace to biomedical diagnostics and beyond.

The digitalization of future engineered systems is directly linked to advances in sensing technology. Higher-resolution, higher fidelity sensing will ultimately drive progress in real-time monitoring, predictive maintenance, and adaptive control across diverse applications[6–9]. Enhancing sensitivity, accuracy, and reliability of current technology is crucial for ensuring safety and operational efficiency of next-generation transportation and energy infrastructure[10–13]. This is particularly critical in the global transition towards a hydrogen-based economy[14–16]. Here traditional sensors in particular, face inherent limitations in extreme environments and pose potential spark ignition risks[17,18].

Since the advent of fiber optic technology, silica-based optical fiber sensors have emerged as a compelling alternative to electronic sensors. Their inherent robustness makes them particularly suited to chemically aggressive, high-temperature, and high-pressure environments[19–21], offering integration advantages through compact size and multiplexing and inherent immunity of the signal to electromagnetic interference. Additionally, embedding multiple sensing elements along a single compact optical fiber reduces cabling, and routing complexity faced by electronic alternatives, significantly simplifying integration into engineered structures. Fiberized devices also offer unprecedented scalability through fiber drawing, permitting cost-effective production of devices that can be easily deployed across diverse applications[22–27].

Optical fibers are typically made by elongating, i.e. drawing a ‘preform’ that contains features that enable the production of desired fiber structure. Commonly, optical fiber preforms are made using vapor-deposition (VD) methods where liquid precursors are oxidized using plasma or oxy-hydrogen flames to form silica-based glass. The traditional fabrication limits the design space of fiber preforms to cylindrical shape[27]. For more complex cross-sections, manual stacking or physical machining of initially circular cross-section preform or fiber is often used[28–31], however it is notoriously labor intensive and time consuming. Optical fibers drawn from such a preform are thin glass cylinders

with a diameter of 125 µm, developed to balance mechanical flexibility and robustness[32]. Although thicker fibers offer greater robustness, flexibility is sacrificed and integration becomes more difficult, especially in the case of embedded sensors. To minimize discontinuities and potential points of failure, thinner fiber sensors are therefore preferred[33,34]. Alternatively, to glass fibers, polymer fibers are often used in sensing applications. However, silica glass-based fibers in comparison to e.g., polymer fibers (typically made of PMMA), offer nearly 25x higher Young Modulus, that enables efficient strain transfer to the sensing elements placed within the fiber core[35–37]. Furthermore, plastic fibers are unsuitable for harsh environments e.g., elevated temperatures that lead to polymer degeneration and premature failure.

Conventional solid glass fibers are effective in measuring strains produced by forces aligned with the fiber axis but are limited in their response to transverse forces. The sensitivity of conventional optical fiber sensors often relies on intrinsic material properties or simple modifications. The current state-of-the-art sensitivity of fiber Bragg gratings in optical fibers is typically in the range of 0.65 pm/MPa[12]. Incorporating microstructure, i.e., air channels running parallel to the waveguide can significantly enhance fiber sensitivity to transverse strain[38]. Nonetheless, even if microstructured fiber is used, the current maximum resolution for pressure sensing is 0.23 MPa[39,40]. Furthermore, the ability to differentiate between stresses in the transverse directions is wholly dependent on the orientation of the fiber being maintained in the sensing application, with even slight twists compromising the ability to distinguish transverse strains. Installing optical fibers without rotation poses significant challenges in real-world applications, demanding meticulous control. To address this issue, a non-circular or even rectangular cross-section would be preferred as the non-circular faces provide a means to control the fiber orientation. Previously, elongated or rectangular cross-sections were achieved through physical machining of round preforms, collapsed drawing, or manual stacking[26,41,42]. However, these methods often resulted in fibers with numerous drawbacks, including increased fiber thickness, challenging scalability and problematic microstructure integration.

In the paper, we present a new class of silica-based optical fiber, termed high-aspect-ratio-flat-fibers (HARFF). Unlike conventional axisymmetric optical fiber, the HARFF is characterized by a quadrilateral target cross-section, and a large width to thickness ratio or aspect ratio (AR) of the order 10:1 or greater. Here, the HARFF-preforms were obtained through advanced laser-based processing[43]. These preforms were then drawn using a traditional fiber-drawing tower to produce over 120 m of continuous HARFF from a single preform. We also demonstrated that the HARFFs are fully compatible with commercial fibers, enabling seamless and straightforward integration into existing optical systems and infrastructure. A key feature of the HARFF is the ability to integrate relatively large laser engineered microstructure in the fiber that enhances and tailors the sensitivity to type of external stimulus. As proof-of-concept, we demonstrated the functionality of the HARFF by utilizing a laser-written Bragg grating -based Fabry-Perot cavity (FP-FBG) design to obtain ultra-sensitive sensors. First, our proof-of-concept 80 µm thick and 655 µm wide microstructured HARFF sensor achieved sensitivity of 0.138 kPa using a standard interrogator, thereby representing over a three orders of magnitude improvement over the earlier mentioned state-of-the-art. Here, using a standard interrogator, we demonstrated 7.24 dB/MPa (peak-to-valley (PV)) sensitivity. Additionally, we demonstrated an improved temperature sensitivity of up to 12 nm/K and 0.075 dB/K using a hybridized i.e., alloy-filled microstructure HARFF sensor. Our advances underscore the transformative potential of HARFFs, setting a new benchmark in ultra-sensitive sensing and paving the way for future innovations in non-circular fiber optics.

2. High-aspect ratio flat fibers

2.1 Fabrication of HARFF

To obtain HARFF preforms, we used a custom-built laser-based glass processing system, which mitigates many limitations of traditional glass-fabrication. High confinement and controlled thermal exposure are essential in fabrication of HARFF, to mitigate surface-tension related deformation of the preform, which cannot be achieved in traditional flame-based methods. The extended versality of our system enables cutting, depositing, and welding of silica-based components to form the preform[43]. The system comprises a CO_2 laser ($\lambda = 10.6$ µm) with maximum output power of 60 W. CO_2-laser based heating, which enables rapid and localized melting of silica-based glass [27,44]. The CO_2 laser beam is shaped by an interchangeable ZeSe lens system to provide a numerical aperture (NA) of the incident beam that can be tuned in the range of 0.05 - 0.10. The main steps involved in fabrication of HARFF preforms are depicted in Fig. 1. First, 1 mm thick flat silica-wafers (XJGS1) were cut to the desired dimensions. Next, the preform

stack was assembled and laser-welded along the edges to create permanent and robust bonds between each component. Furthermore, selective welding allows the definition of the channel geometry in the HARFF. Thereby, it is possible to make single or multi-channel configurations, essential in the manufacturing process of microstructured HARFF (termed μHARFF). The glass-to-glass welds allow the channels to be pressurized during fiber drawing, so that the shape and fiber thickness, as exampled in Fig. 1 (d,e) can be controlled. To create the joint between the components in the stack, a spot size of approximately 2 mm and a laser power of up to 60 W was used. Welding was performed at a speed of 0.5 mm/s. Upon exposure to the laser beam, the energy was absorbed by the components, causing them to soften locally, resulting in a localized *melt pool*. The reduced viscosity and surface tension of the softened glass allow the reflow of the material filling any gaps or spaces between the components, creating a continuous joint. As the material cools and solidifies, a durable and airtight weld is formed between the components. Lastly, a circular silica-tube (OD of 10 mm) was similarly laser-welded at the top of the preform to provide a mounting handle for a standard chuck of the fiber draw tower. The tube was also used to mitigate pressure buildup through a pressure-feedback system to maintain constant atmospheric pressure in the microstructure during the drawing process. In our experiments, the assembled preforms typically were 33 mm wide, which was dictated by the maximum aperture of the available draw-tower furnace.

The preform was drawn into HARFF using a conventional draw tower with a conductive furnace with an aperture of 35 mm. The furnace was used to heat up the lower end of the preform to a drawing temperature of approximately 1960°C. The preform was fed into the furnace at a speed of 1 mm/min, while the capstan speed was ramped up to 1.5 m/min. Before collecting the fiber onto the capstan, a UV-curable protective coating (ORMOCER CBS-106) was applied to the fiber via atomizers and cured. Using the abovementioned method, over 120 m of continuous HARFF was drawn from a single preform. This length was limited by the relatively short, 150 mm, length of the proof-of-concept preforms.

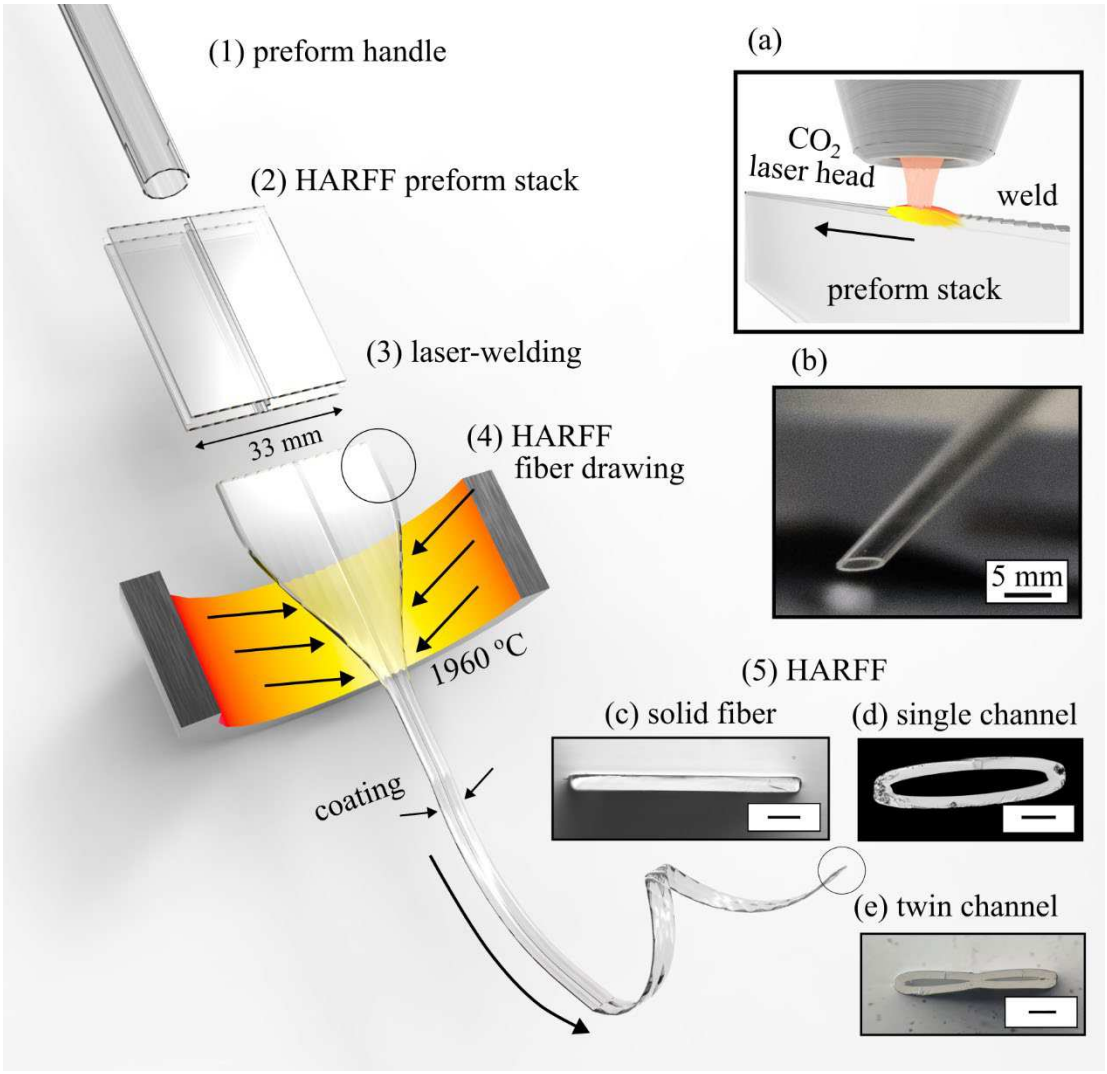

Fig. 1 Schematic of fabrication of HARFF: (1-2-3) preform stacking and laser-welding ((a) laser-weld used to seal the sides of the stack); (4) fiber drawing in traditional conductive optical fiber draw tower ((b) micrograph of typical cross-section through neckdown of single-channel preform), and (5) example cross sections of (c) solid and (d,e) microstructure HARFFs. The scale bars correspond to 80 µm.

2.2 Design considerations for microstructure HARFF

A key mechanical advantage of HARFF over conventional axisymmetric fibers lies in its flexural rigidity. Fig. 2 shows a comparison of the cross-section shape of the conventional HARFF and µHARFF optical fibers. The plot shows the second moment of area about the lateral axis (I_x), for an 800 µm wide HARFF to that of circular fibers, demonstrating that HARFF is generally more rigid than circular fiber of the same thickness. Notably, HARFF with a thickness of approximately 55 µm exhibits comparable lateral flexural rigidity to standard 125µm diameter optical fibers. For thicker HARFFs i.e., > 100 µm, I_x is comparable to the common large diameter round fibers 250 µm. This ensures that even thicker HARFF are both rigid, while being flexible enough to be wound. The latter is pivotal in terms of scalability of any specialty fiber. Lastly, the vertical second moment of area (I_y) can be tailored independently by adjusting the width for any given desired thickness, an approach not feasible for axisymmetric fiber. Moreover, the rectangular cross-section of HARFF mitigates buckling and twisting common in the case of circular fibers.

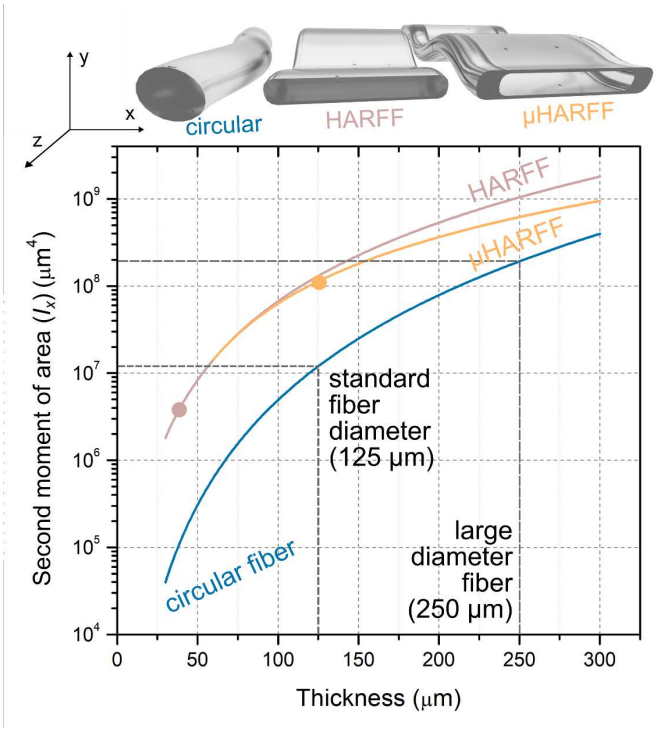

Fig. 2 Comparison of the Second moment of Area (I_x) between circular fiber and 800 μm wide HARFF; in the case of microstructure HARFF (μHARFF), the wall thickness of 30 μm was used.

The unique optical properties of μHARFF enable ultra-sensitive sensing capabilities by leveraging strain-induced birefringence within an optical waveguide. For a waveguide aligned along z-axis, the birefringence, B, is governed by microstructure-induced strain and is defined as[45]:

$$B = n_2 - n_3 = \frac{n_0^3}{2}(p_{11} - p_{12})(\epsilon_{33} - \epsilon_{22}) \quad (1)$$

where n_2 and n_3 are the effective refractive indices of the optical waveguide for orthogonal polarization states, when electric field is aligned to the x-axis and y-axis respectively. The effective refractive index, n_o, is for an assumed geometrically symmetric waveguide under no external stress, p_{11} and p_{12} are the strain-optic coefficients, 0.121 and 0.270 respectively for fused silica. The maximum and minimum principal strains in the plane transverse to the fiber axis are represented by ϵ_{33} and ϵ_{22}, respectively.

A Finite element method (FEM) model was constructed to predict the sensitivity of the birefringence response of μHARFF microstructure. By tailoring the μHARFF cross-sectional geometry, birefringence sensitivity can be optimized for specific sensing applications, such as pressure or temperature measurement. The role of FEM study was two-fold: (*i)* predict the sensor's birefringent response to hydrostatic pressure and *(ii)* establish design guidelines for optimizing sensitivity through a geometric parameter sweep.

(i) Predicting birefringent response to hydrostatic pressure; The cross-section of a μHARFF sensor is shown in Fig. 1 (e). The corresponding parametric shape to represent this cross-section, developed for the FEM studies, is shown in Fig. 3 (a). The cross section is defined by the width and height (w, h), wall thickness (t), and microstructure spacing (δx). This shape was used to create a simple plane strain linear elastic model using CPE4R elements, which simulated hydrostatic pressure by applying 0.1 MPa and 0.5 MPa to the internal and external surfaces, respectively. A Young's modulus of 73 GPa and a Poisson's ratio of 0.2 was used for silica glass material properties. The methodology and python scripts for generating/meshing the parametric geometry and for performing the mesh sensitivity study are provided in the supplementary information (DOI: *Insert DOI here*).

The unique design of the µHARFF provides a significant improvement over previous microstructured optical fibers[38,45] by enhancing the birefringent response, i.e. the difference in the principal strains ($\varepsilon_{diff} = \varepsilon_{33} - \varepsilon_{22}$, see Equation 1). The improvement is due to the hollow elongated cross-section which enables a greater deflection in the in the y-direction and makes the sensor more responsive to the pressure load. The color maps in Fig 3. (b) and Fig 3 (c) show the strains in the x and y-directions (ε_{xx} and ε_{yy}), which were used in conjunction with the shear strain (ε_{xy}) to calculate the maximum and minimum principal strains (ε_{33} and ε_{22}). Fig. 4 (a) shows a plot of ε_{22}, ε_{33} and ε_{diff} against the x-axis position along Lines 1 and 2 in Fig. 3(a). Choosing the positioning of the waveguide in the cross-section means making a tradeoff between maximizing ε_{diff} and minimizing signal losses.

The high values of ε_{diff} at the tips of the microstructure result from an assumed tip radius of 0.25 µm. However, the high strain gradients at these positions, as well as the adjacency to the fibre surface, which would cause mode cut off due to evanescent field exposure, make these regions unsuitable to position the waveguide. The plots in Fig. 4 (a) enable the positioning of the waveguide in the region where ε_{diff} relatively high and stable: at $x = 0$ on Line 1.

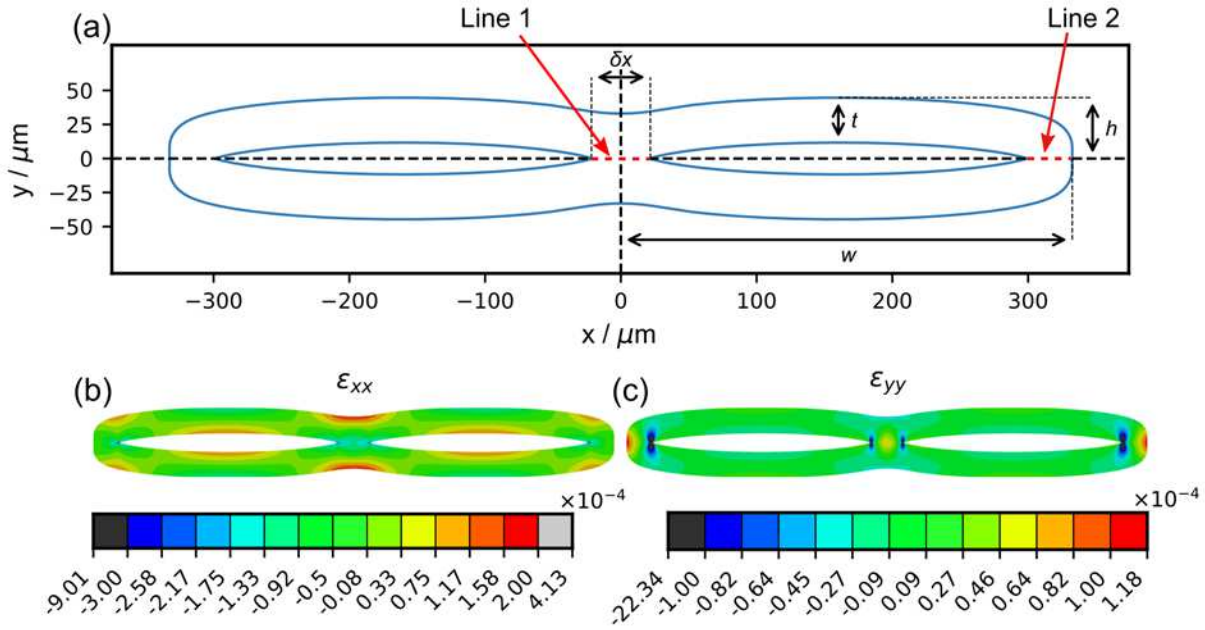

Fig. 3 Generated quadrilateral geometry (a) representing µHARFF shown in Fig, 1 (e), and (b,c) Colormaps showing FEM simulation results of ϵ_{xx} vs ϵ_{yy} strain in twin-channel µHARFF.

(ii) Geometry parameters sweep study for Next-Generation µHARFF sensors: Since the µHARFF cross-section was parameterized in the FEM, a parametric study was conducted to explore design iterations to optimize sensitivity and provide target geometries for future devices. The methodology and python scripts for the parametric study are provided in the supplementary information (DOI: *Insert DOI here*). Here, the values of w, h, t, and δx were varied to produce µHARFF geometries of different aspect ratios and wall thicknesses. Each key parameter was varied over a specific range (± 50%) centered on the baseline values (Fig. 3 (a)) using a fixed number of five intervals.

Regression coefficients were calculated by fitting a linear model to normalized input parameters (w, h, t, and δx) and the target variable (ε_{diff} value at the centre of the cross-section), minimizing the squared error to estimate each parameter's relative influence. The spider plot in Fig. 4 (b) visualizes these coefficients, where the distance along each axis represents the strength and direction of sensitivity - showing which input parameters most strongly affect the target and whether their influence is positive or negative. The plot shows that the sensor responds most strongly to reducing the wall thickness *(t)* and increasing the width *(w)*, confirming that creating high aspect ratio µHARFF designs provides ultra-high sensitivity to bi-axial strain.

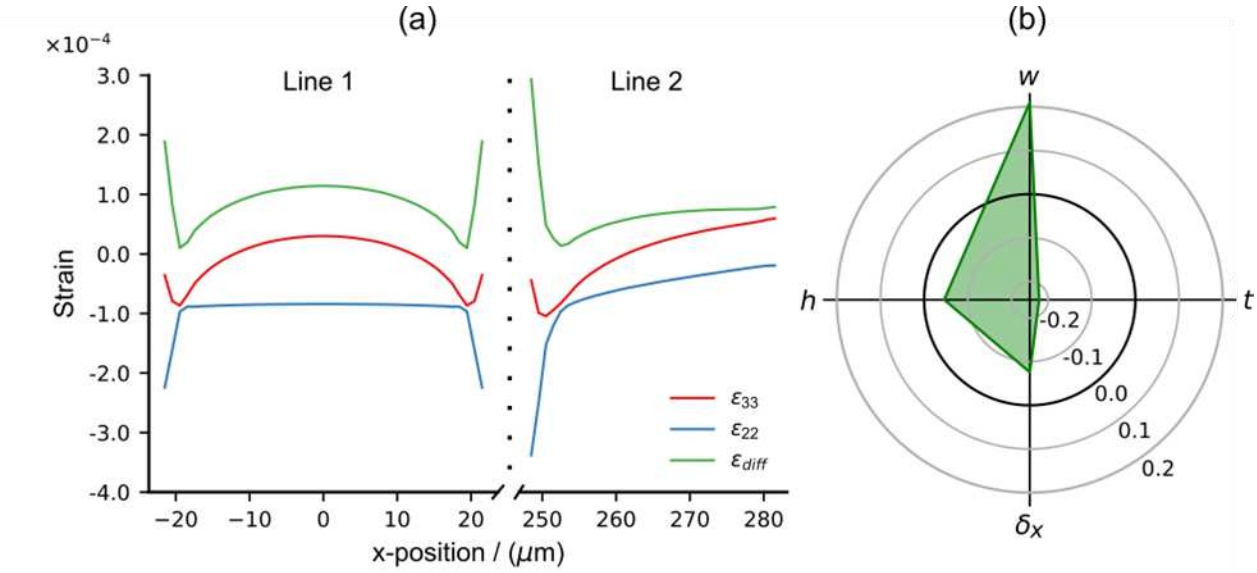

Fig. 4 (a) Plots of the principal strains (ε_{22}, ε_{33}) and strain differences (ε_{diff}) against x-position along Lines 1 and 2 (see Fig. 3 (a)) and, (b) summary of sensitivity analysis i.e., ε_{diff} obtained in the waveguide for the cross-sections

3. Experimental Results - Sensitivity of high-aspect-ratio flat fibers

To highlight unique features of HARFF, and as proof-of-concept we implemented a single- and twin-channel µHARFF demonstrating enhancements in *(i)* pressure and *(ii)* temperature sensing. Sensor operation is based on externally induced deformation of the optical fiber that results in a change of the induced birefringence of the waveguide (see Eq. 1). To interpret the birefringence response, our sensor contained two spatially separated but identical period fiber Bragg gratings (FBGs). As these gratings were of similar period, a Fabry Perot cavity was formed between them. When unpolarized light was launched into the cavity the summation of these spectra can be used as a means to infer changes of birefringence, by means of a Vernier effect[46]. For example, the pressure-induced strain of the HARFF alters the birefringence in the waveguide to affect each polarization's effective mode index differently. The peak/valley (PV) power levels of the resulting spectra thus varied as external load, here, pressure or temperature was changed. It should be noted that this comes in addition to the inherent sensitivity improvement provided by the fiber design. In Fig. 1 (c-e) three different versions of HARFF are shown. In the scope of this work, we underlined development and potential applications of high-aspect-ratio microstructure enabled by HARFF, it is noteworthy however that solid fibers (see Fig. 1 (c)) have recently demonstrated application as a platform for achieving high stability speckle-based optical interrogator[47].

(i) HARFF-based pressure sensor: To obtain the sensor, a short section of uncoated twin-channel µHARFF was cleaved using a commercial cleaver equipped with a diamond blade and then the microstructure was sealed on both ends. To seal the microstructure, a single CO_2 laser pulse (t = 1 s) was used to melt the end of the fiber and allow viscous forces to close the channels. Subsequently, a commercial single-mode fiber (SMF-28e+, Corning Inc) was spliced using a laser-splicer (LZM-100, Fujikura Ltd). The splicer was equipped with a custom-made holder, that enabled 5-axis alignment of the HARFF in respect to the round fiber. To mitigate the signal-coupling losses due to possible deformation of the SMF core, a short piece (< 1mm) of 125 µm coreless silica-fiber was spliced in between SMF and HARFF as shown in Fig. 5. The following splicing recipe was used: (i) initial alignment of the round fiber to the desired position on HARFF with the gap of approximately 10 µm, (ii) simultaneous melting of both fibers by an incident laser beam, (iii) contacting the molten fibers and then (iv) tapering of the splice. The parameters were experimentally optimized for repetitive and robust joints between the fibers and fine-tuned for different HARFF designs. During splicing, the microstructure collapsed due to viscous forces creating two sealed air pockets as depicted in the inset in Fig. 5.

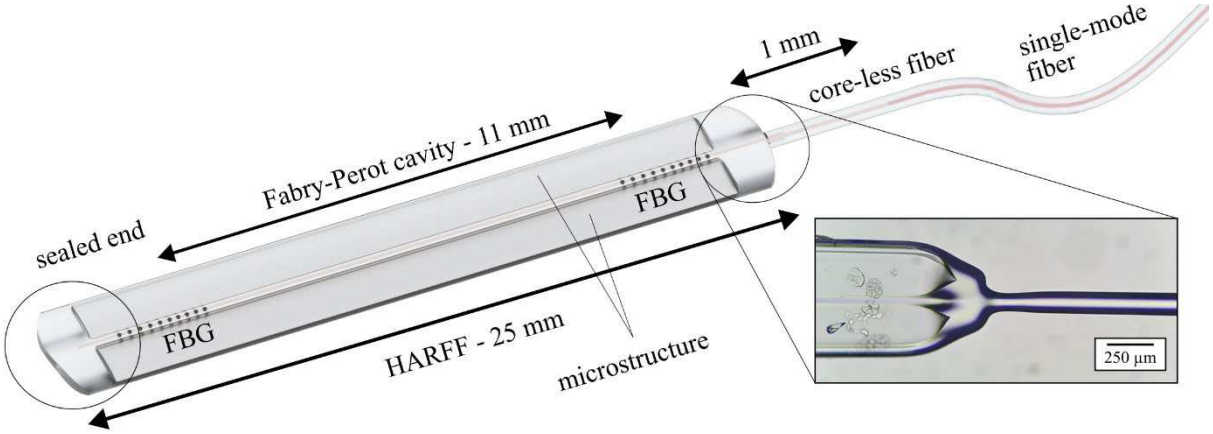

Fig. 5 Schematic of HARFF-based sensors (not to scale); the inset shows a micrograph of the splice between commercial round fiber and microstructure HARFF.

An interferometric sensor was fabricated at the center of the prepared sample, utilizing a pair of FBGs inscribed in a vertically and laterally centered waveguide, which was seamlessly connected to SMF through a coreless fiber section. These optical structures were fabricated using a femtosecond laser writing system[48] consisting of a Yb:KGW laser (λ=1030 nm, 200 fs pulses at 200 kHz, PHAROS, Light Conversion) that was frequency doubled by a BBO crystal, resulting in a λ = 515 nm second harmonic inscription beam. A quarter waveplate was used to produce circular polarization to ensure a smooth refractive index change while mitigating nanograting damage formation which could lead to high polarization dependent losses[49]. The beam was focused using a ×50 immersion objective of variable NA 0.5-0.9 (PLN50XOI, Olympus) into the µHARFF, using an n = 1.53 immersion oil (Laser Liquid, Cargille). First, the waveguide with a rectangular cross-section i.e., 10 by 8 µm was written by rastering 50 scanlines at 200 nm lateral separation in a multiscan pattern [50] with a scanline pulse density $D = 3\times10^5$ pulses/mm, pulse energy E_p = 50 nJ and objective set to 0.5 NA. This induces an estimated index change $\Delta n \sim 3\times10^{-3}$ based on previous work [48]. Note that waveguide birefringence arises not only from the rectangular geometry, but also from laser-induced local strain anisotropy. Subsequently, two FBGs were inscribed in the waveguide using point-by-point method[51]. The objective NA was set to 0.9, and each point was written by firing a single pulse ($E_p \sim$ 90 nJ). A period of 2.1 µm was chosen, which corresponds to a 4th order λ =1550 nm grating. Each FBG was 3 mm long with an 11 mm separation between their midpoints. The cavity length corresponds to a ~80 pm FSR, which ensured visibility of spectral fringes on the spectrum analyzer used for in-situ characterization during fabrication (20 pm resolution, Yokogawa AQ6370D) as well as most standard interrogators. The thereby formed cavity was longitudinally centered in µHARFF to minimize the impact of the bulky, collapsed ends where pressure sensitivity would be relatively weaker.

The sensor was installed in a test pressure vessel capable of pressurizing up to 0.40 MPa. The pressure was monitored with a manometer, accurate to ±0.02 MPa. For sensor interrogation, a wideband Er-doped amplified spontaneous emission source was utilized. The signal, at approximately $\lambda_s \approx$ 1550 nm, was coupled through one branch of a 3 dB splitter, with the other branch connected to an optical spectrum analyzer (Yokogawa AQ6370D). Spectral resolution was up to 0.02 nm. The PV shift of the center fringe (see Fig. 6 (a-c)) was up to 7.24 dB/MPa, with a minor hysteresis of up to 0.06 dB noticed at atmospheric pressure. To evaluate any temperature influence on the readings, in Fig. 6 (d-

f) the thermal response of the sensor is shown. The spectral shift in temperature was typical for an FBG in silica-based fibers[52]. The PV change in temperature was in order of 10^{-3} dB/K.

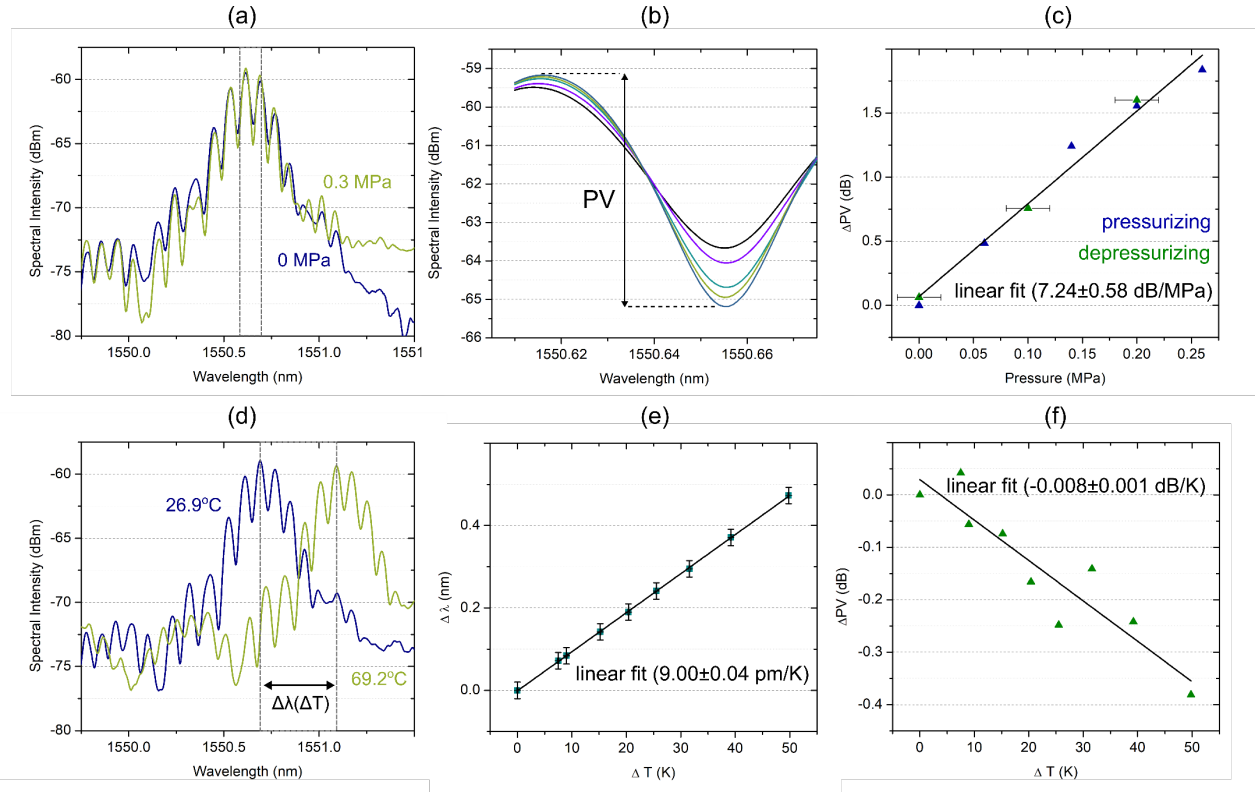

Fig. 6 Spectral response of (a) µHARFF-based pressure sensor with visible fringes, (b) typical PV change for different pressures (see the dashed fringe in (a)), and (c) linear fit of pressure sensitivity during pressurizing (in blue) and depressurizing the vessel (in green). Spectral shift (d) of the center fringe in elevated temperatures, and (e) it corresponds to 9 pm/K (linear fit) with minor (f) PV change.

(ii) µHARFF-based temperature sensor: To enhance the temperature sensitivity and maximize PV response, the single-channel µHARFF was filled, post-draw, with Sn-based alloy ($T_{melting} \approx 220$ °C); a micrograph of the alloy filled fiber is shown in Fig. 7 (a). The waveguide and sensor structure (as described in Fig. 5) was written in the side wall of the µHARFF. Thereby, the birefringence change was enhanced by the thermal expansion coefficient difference between the alloy and the silica-based fiber. The sensor was placed on DC-controlled heating element, while the temperature was monitored with a thermocouple. Fig. 7 (b) shows a selection of fringe evolutions for different temperatures. The increasing temperatures effected the red shift as well as the change of the fringe contrast (ΔPV); both were in line with our expectations. The change in the fringe contrast showed a periodic sign change, first at around $\Delta T \approx 13$ K. In comparison to the twin-channel µHARFF, alloy-filled single-channel µHARFF showed a 50 % higher spectral shift of up to 12.1 pm/K. The PV temperature sensitivity was an order of magnitude higher in comparison to the twin-air-channel HARFF discussed earlier, up to ±0.075 dB/K, as shown in Fig. 7 (c).

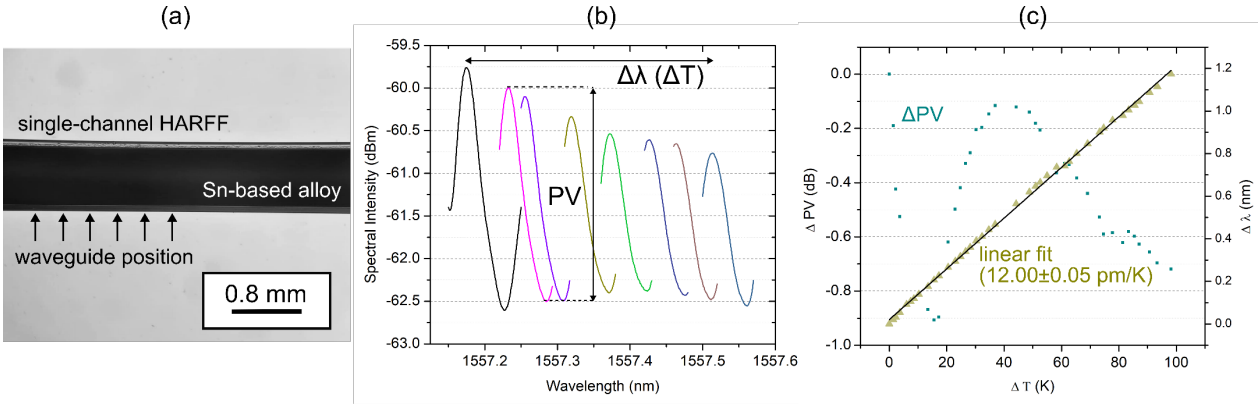

Fig. 7 Micrograph (a) of alloy filled sensor based on a single channel HARFF (bottom illumination used); (b) spectral response of the sensor, and (c) its sensitivity demonstrated up to 12 pm/K and ±0.075 dB/K in 20 K periods.

4. Discussion

We have showcased the opportunities linked to non-circular high-aspect ratio flat fibers. In the case of solid HARFF, shown in Fig. 1 (c), our manufacturing approach allowed an ultra-high AR to be obtained of up to approximately 20:1 and high flatness of the cross-section with maximum top-bottom surface variations of less than 1 µm, measured with optical profiler (ZeGage™ Pro HR 3D). The initial preform AR was 33:1, limited by commercially available wafer dimensions and the aperture of the draw tower furnace. The discrepancy between ARs of the preform and the resultant fiber may be attributed to surface tension and viscous forces in the neck-down region during the drawing. In the future alternative drawing strategies will be explored to further increase the HARFF shape control.

As proof-of-concept of potential application of µHARFF we developed two types of ultra-sensitive sensors that leverage enhanced birefringence in two types of fibers, single- and twin-channel. In the case of twin-channel pressure sensor, we obtained up to three orders of magnitude sensitivity improvement over the earlier reported devices based on silica-fibers[37,40]. Such sensitivity translates to ease of use, allowing these sensors to be used with less-sensitive, lower cost interrogators in real-life applications. The µHARFF can also be hybridized by e.g., filling the channels with various materials, thus creating hybridized fiber sensors. For our demonstration case, we used a low melting temperature Sn-based alloy, however other alloys with higher melting temperature can be used to further increase working range. The contrast of the fringes changed periodically with temperature due to the well-documented Vernier effect[46]. Such a response over a small temperature range, i.e. $\Delta T \approx 13$, indicates that strong birefringence was induced in the waveguide. This made possible only by the large µHARFF channel which could be filled with metal to provide the thermal expansion coefficient difference between silica and the alloy. It is noteworthy that the exact geometry of µHARFF sensor can be further optimized to increase or linearize its sensitivity, by e.g., shape optimization or increasing metal-to-glass ratio in the cross-section. Nonetheless, our results can be considered as a strong proof-of-concept, noting that further optimization will be the object of future work. Despite this, the simulations showing strong µHARFF birefringence response to external stimulus (shown in Section 2.2) align with our results. This reinforces confidence in our model and highlights the necessity of high AR designs to amplify sensitivity and improve performance in such sensors.

The newly introduced HARFF fibers represent a novel class of specialty optical fibers with cross-disciplinary advantages. The enhanced second moment of area, as illustrated in Fig. 2 significantly improves manual handling of thin HARFF fibers while remaining highly flexible and sensitive. The unidirectional rigidity of HARFF enables precise strain decoupling, making it particularly beneficial for sensing applications requiring directional sensitivity. Furthermore, the quadrilateral cross-section of HARFF mitigates buckling and twisting that is typical for round fibers. HARFF is an ultra-thin and ultra-flexible optical fiber in the thickness dimension, while offering high stiffness and structural integrity in the other dimension due to its width. HARFFs also importantly offer greater versatility for internal microstructure, as their wide geometry offers a lateral degree of freedom for design unavailable in traditional circular fibers, which are constrained by their limited diameter. The development of elongated microstructure, realized through the µHARFF fabrication approach, unlocks ultra-high strain sensitivity in the plane normal to waveguide

propagation direction that is commonly challenging to attain using traditional fibers[39]. In our simulations and experiments, i.e., temperature and hydrostatic pressure sensing, we showed that the birefringence obtained in µHARFF can be used to monitor multi-parameter loads regardless of their direction. Lastly, the unique geometry i.e., highly flat faces and significant width of HARFF presents an exciting opportunity for novel multi-disciplinary platforms that can be leveraged in microfluidic, fiberized integrated planar photonic devices, ultra-sensitive distributed sensing, power scaling, higher-order-mode communication and more.

5. Conclusion

In this work, we introduced a new class of fiber optics with non-circular, quadrilateral target cross-section that are fully compatible with commercial fibers. The latter means they can be easily integrated with the existing fiber systems and infrastructure. By leveraging laser-based manufacturing techniques we mitigated many limitations that are linked to traditional fiber preform manufacturing routes. Through the means of traditional fiber drawing, we fabricated a range of over 100 m long continuous high-aspect ratio flat fibers (HARFF), with a few examples of attainable microstructure. The microstructure was pre-designed using finite-element-analysis to maximize birefringence change upon fiber perturbation. The demonstrated examples of high-sensitivity HARFF included single and twin-channel microstructure. As proof-of-concept we examined sensors that show up to three orders of magnitude improvement to differential pressure, over earlier reported devices with further improvements in case of alloy-filled HARFF for temperature sensing. In this work, we focused on discrete sensors that are based on short sections of various HARFF, while the demonstration of distributed sensing is planned in the future. The results discussed in this paper underline the opportunities brought about by HARFF using set demonstrators, however the potential of this fiber type extends beyond applications here demonstrated, including microfluidics, lab-on-fiber, optoelectronics and more.

Author contribution

PM, BM and CH fabricated the HARFFs presented in this work, RH, MW and CH prepared FEM analysis, PM and CH designed the FP-FBG based sensing structure, PM and TL developed recipes for round-fiber integration with HARFF, TL and MB wrote FP-FBG, PM characterized the sensors and wrote the manuscript, all authors took part in result analysis and review of the manuscript.

Acknowledgements

The authors express their gratitude to Nicholas White, Glenn Churchill, Meisam Jalalvand, and Benjamin Hatfield for their invaluable technical support and acknowledge Sir David Payne and Francesco Poletti for their valuable insights and guidance during discussions that helped shape this work.

Authors acknowledge funding from Engineering and Physical Sciences Research Council (EP/Y016920/1), Swedish Research Council (Vetenskapsrådet) (2022-06180), Stiftelsen Tornspiran (1031).

Disclosures

The authors declare no conflict of interest.

The methodology and python scripts for generating/meshing the parametric geometry and for performing the mesh sensitivity study described in Section 2.2 are provided in the supplementary information (DOI: *Insert DOI here*).

Data underlying the results presented in this paper are not publicly available at this time but may be obtained from the authors upon reasonable request.

References

1. Sato, S., Kawaguchi, Y., Sakuma, H., Haruna, T. & Hasegawa, T. Record Low Loss Optical Fiber with 0.1397 dB/km. in *Optical Fiber Communication Conference (OFC) 2024* Tu2E.1 (Optica Publishing Group, Washington, D.C., 2024). doi:10.1364/OFC.2024.Tu2E.1.

2. Knall, J. *et al.* Radiation-balanced silica fiber laser. *Optica* **8**, 830 (2021).

3. Blanc, W., Tosi, D., Leal-Junior, A., Ferrari, M. & Ballato, J. Are low- and high-loss glass–ceramic optical fibers possible game changers? *Opt Commun* **575**, 131300 (2025).

4. Blanc, W. *et al.* The past, present and future of photonic glasses: A review in homage to the United Nations International Year of glass 2022. *Prog Mater Sci* **134**, 101084 (2023).

5. Chen, Y. *et al.* Hollow Core DNANF Optical Fiber with <0.11 dB/km Loss. in *Optical Fiber Communication Conference (OFC) 2024* Th4A.8 (Optica Publishing Group, Washington, D.C., 2024). doi:10.1364/OFC.2024.Th4A.8.

6. Irfan, M. S., Khan, T., Hussain, T., Liao, K. & Umer, R. Carbon coated piezoresistive fiber sensors: From process monitoring to structural health monitoring of composites – A review. *Compos Part A Appl Sci Manuf* **141**, 106236 (2021).

7. Min, R. *et al.* Optical fiber sensing for marine environment and marine structural health monitoring: A review. *Opt Laser Technol* **140**, 107082 (2021).

8. Elsherif, M. *et al.* Optical Fiber Sensors: Working Principle, Applications, and Limitations. *Adv Photonics Res* **3**, (2022).

9. Kandemir, K., Guinchard, M., Crouvizier, M., Sacristan, O. & Mugnier, S. Distributed optical strain sensing measurements down to cryogenic temperatures. *Appl Opt* **62**, E125 (2023).

10. Miliou, A. In-Fiber Interferometric-Based Sensors: Overview and Recent Advances. *Photonics* **8**, 265 (2021).

11. Deng, Y. & Jiang, J. Optical Fiber Sensors in Extreme Temperature and Radiation Environments: A Review. *IEEE Sens J* **22**, 13811–13834 (2022).

12. Sulejmani, S. *et al.* Shear stress sensing with Bragg grating-based sensors in microstructured optical fibers. *Opt Express* **21**, 20404 (2013).

13. Martynkien, T. *et al.* Highly birefringent microstructured fibers with enhanced sensitivity to hydrostatic pressure. *Opt Express* **18**, 15113 (2010).

14. Sambo, C. *et al.* A review on worldwide underground hydrogen storage operating and potential fields. *Int J Hydrogen Energy* **47**, 22840–22880 (2022).

15. Züttel, A. Materials for hydrogen storage. *Materials Today* **6**, 24–33 (2003).

16. Ashry, I. *et al.* A Review of Distributed Fiber–Optic Sensing in the Oil and Gas Industry. *Journal of Lightwave Technology* **40**, 1407–1431 (2022).

17. Luo, Y. *et al.* Technology Roadmap for Flexible Sensors. *ACS Nano* **17**, 5211–5295 (2023).

18. Fuchs, S. *et al.* In-Line Analysis of Organ-on-Chip Systems with Sensors: Integration, Fabrication, Challenges, and Potential. *ACS Biomater Sci Eng* **7**, 2926–2948 (2021).

19. Deng, Y. & Jiang, J. Optical Fiber Sensors in Extreme Temperature and Radiation Environments: A Review. *IEEE Sens J* **22**, 13811–13834 (2022).

20. Wang, Y. *et al.* 3D Laser Engineering of Molten Core Optical Fibers: Toward a New Generation of Harsh Environment Sensing Devices. *Adv Opt Mater* **10**, (2022).

21. Miele, E. *et al.* Hollow-core optical fibre sensors for operando Raman spectroscopy investigation of Li-ion battery liquid electrolytes. *Nat Commun* **13**, 1651 (2022).

22. Jia, Y. *et al.* Low frequency vibration monitoring of wind turbine tower based on optical fiber sensor and its potential for internet of things. *Sens Actuators A Phys* **379**, 115891 (2024).

23. Vaiano, P. *et al.* Lab on Fiber Technology for biological sensing applications. *Laser Photon Rev* **10**, 922–961 (2016).

24. Roldán-Varona, P., Rodríguez-Cobo, L. & López-Higuera, J. M. Reflection-based lab-in-fiber sensor integrated in a surgical needle for biomedical applications. *Opt Lett* **45**, 5242 (2020).

25. Berthold, J. W. INDUSTRIAL APPLICATIONS OF FIBER OPTIC SENSORS. in *Fiber Optic Sensors* 573–591 (Wiley, 2024). doi:10.1002/9781119678892.ch22.

26. Strutynski, C. *et al.* Stack-and-Draw Applied to the Engineering of Multi-Material Fibers with Non-Cylindrical Profiles. *Adv Funct Mater* **31**, (2021).

27. Maniewski, P. *et al.* Advances in laser-based manufacturing techniques for specialty optical fiber. *Journal of the American Ceramic Society* **107**, 5143–5158 (2024).

28. Murphy, L. R., Yerolatsitis, S., Birks, T. A. & Stone, J. M. Stack, seal, evacuate, draw: a method for drawing hollow-core fiber stacks under positive and negative pressure. *Opt Express* **30**, 37303 (2022).

29. Ross, C. A. *et al.* Axi-Stack: a method for manufacturing freeform air-silica optical fibre. *Opt Express* **32**, 922 (2024).

30. Henkel, S., Binder, M., Knauf, M., Bliedtner, J. & Rädlein, E. Influence of ultrasonic tool oscillation during drilling of fused silica. *Advanced Optical Technologies* **13**, (2024).

31. Yuan, T., Zhang, X., Xia, Q., Wang, Y. & Yuan, L. A Twin-Core and Dual-Hole Fiber Design and Fabrication. *Journal of Lightwave Technology* **39**, 4028–4033 (2021).

32. Finn, B. S. *City of Light: The Story of Fiber Optics (Review)*. vol. 43 (2002).

33. Chowdhury, N. T., Wang, J., Chiu, W. K. & Yan, W. Predicting matrix failure in composite structures using a hybrid failure criterion. *Compos Struct* **137**, 148–158 (2016).

34. Rocha, H., Semprimoschnig, C. & Nunes, J. P. Sensors for process and structural health monitoring of aerospace composites: A review. *Eng Struct* **237**, 112231 (2021).

35. Holmes, C., Godfrey, M., Mennea, P. L., Zahertar, S. & Dulieu-Barton, J. M. Flexible photonics in low stiffness doped silica for use in fibre reinforced polymer composite materials. *Opt Mater (Amst)* **134**, 113133 (2022).

36. Ferreira, M. F. S. *et al.* Fabry-Perot cavity based on polymer FBG as refractive index sensor. *Opt Commun* **394**, 37–40 (2017).

37. Statkiewicz-Barabach, G., Kowal, D., Szczurowski, M. K., Mergo, P. & Urbanczyk, W. Hydrostatic Pressure and Strain Sensitivity of Long Period Grating Fabricated in Polymer Microstructured Fiber. *IEEE Photonics Technology Letters* **25**, 496–499 (2013).

38. Anelli, F. *et al.* Design of Microstructured Flat Optical Fiber for Multiaxial Strain Monitoring in Composite Materials. *Journal of Lightwave Technology* **40**, 5986–5994 (2022).

39. He, J. *et al.* Temperature-insensitive directional transverse load sensor based on dual side-hole fiber Bragg grating. *Opt Express* **29**, 17700 (2021).

40. Liu, T. *et al.* 3D Structured Optical Fiber Pressure Sensors. *Journal of Lightwave Technology* **42**, 6375–6380 (2024).

41. Webb, A. S. *et al.* MCVD planar substrates for UV-written waveguide devices. *Electron Lett* **43**, 517–519 (2007).

42. Huang, S., Li, M., Garner, S. M., Li, M.-J. & Chen, K. P. Flexible photonic components in glass substrates. *Opt Express* **23**, 22532 (2015).

43. Maniewski, P., Laurell, F. & Fokine, M. Quill-free additive manufacturing of fused silica glass. *Opt Mater Express* **12**, 1480–1490 (2022).

44. Healy, N. *et al.* CO_2 Laser-Induced Directional Recrystallization to Produce Single Crystal Silicon-Core Optical Fibers with Low Loss. *Adv Opt Mater* **4**, 1004–1008 (2016).

45. Narasimhamurty, T. S. *Photoelastic and Electro-Optic Properties of Crystals*. (Springer US, Boston, MA, 1981). doi:10.1007/978-1-4757-0025-1.

46. Gomes, A. D., Bartelt, H. & Frazão, O. Optical Vernier Effect: Recent Advances and Developments. *Laser Photon Rev* **15**, (2021).

47. Falak, P. *et al.* Compact high-resolution FBG strain interrogator based on laser-written 3D scattering structure in flat optical fiber. *Sci Rep* **13**, 8805 (2023).

48. Lee, T., Sun, Q., Beresna, M. & Brambilla, G. Low bend loss femtosecond laser written waveguides exploiting integrated microcrack. *Sci Rep* **11**, 23770 (2021).

49. Lu, J. *et al.* Fiber nanogratings induced by femtosecond pulse laser direct writing for in-line polarizer. *Nanoscale* **11**, 908–914 (2019).

50. Nasu, Y., Kohtoku, M. & Hibino, Y. Low-loss waveguides written with a femtosecond laser for flexible interconnection in a planar light-wave circuit. *Opt Lett* **30**, 723 (2005).

51. Marshall, G. D., Williams, R. J., Jovanovic, N., Steel, M. J. & Withford, M. J. Point-by-point written fiber-Bragg gratings and their application in complex grating designs. *Opt Express* **18**, 19844 (2010).

52. Kersey, A. D. *et al.* Fiber grating sensors. *Journal of Lightwave Technology* **15**, 1442–1463 (1997).